Draft version January 1, 2013
Preprint typeset using LaTeX style emulateapj v. 12/16/11

THE AQUARIUS STREAM PROGENITOR WAS NOT A GLOBULAR CLUSTER: ITS HISTORY COULD BE FAR MORE INTERESTING[1]

Andrew R. Casey[2,3] and distinguished collaborators

Draft version January 1, 2013

ABSTRACT

We present a detailed dynamic and chemical analysis of 5 Aquarius stream giants observed using the MIKE spectrograph on the Magellan Clay Telescope. Assuming all candidates are stream members, our data indicate the Aquarius stream has a large metallicity dispersion. We find no Na-O anti-correlation, and no chemical evidence that the stream is a result of a disrupted globular cluster, contrary to Wylie-de Boer et al. (2012).

Subject headings: Galaxy: halo, structure — Individual: Aquarius Stream — Stars: FGK-giants

1. INTRODUCTION

Galaxies are formed hierarchically through chaotic mergers of smaller systems. The Milky Way is no exception. In our own stellar halo, we see ongoing evidence of these accretion events. As accreting satellites infall onto the galaxy, tidal forces disrupt the dwarf, hurtling stars in leading and trailing streams. The phase space information of stars within such streams are sensitive to the galactic potential. They can collectively constrain the fraction and distribution of accreted matter in the stellar halo, the sub-halo mass function, as well as the shape and extent of dark matter in the Milky Way. Moreover, individual chemical abundances can constrain the precise nucleosynthesis sites where elements are forged, and can collectively trace the chemical evolution of the galaxy.

Wide-field surveys have proved excellent sources for finding stellar streams. Dozens of streams reaching out up to 150 kpc in the halo have been identified through photometric selections and matched-filtering techniques (**??**). Indeed, it is clear that a large fraction of the stellar halo has been built up by accretion. However, as Helmi & White (1999) point out, these observing strategies are only successful for identifying streams that are sufficiently distant from the solar neighbourhood. A nearby stream, within ~ 10 kpc, will not appear as an on-sky over-density, as the stars would be sparsely positioned across the sky. Such substructures would only be detectable by their kinematics, or perhaps precise chemical abundances through a 'chemical tagging' approach (e.g. see **?**).

It is therefore necessary to survey solar neighbourhood stars with spectroscopy in order to detect any nearby substructures. The RAVE (Radial Velocity Experiment) began such a survey in 2003 and has observed spectra from over 500,000 stars across 17,000 deg^2. As the name suggests, the primary goal of RAVE was to obtain radial velocities for the solar neighbourhood and beyond. In an attempt to remain kinematically unbiased, RAVE candidates were selected based only on their apparent magnitude. With the exception of bulge stars, where some photometric cuts were employed, all stars between $9 < \mathrm{I} < 13$ were observed. Almost all of these candidates have published radial velocity measurements (Steinmetz et al. 2006), and for a subset of stars with sufficient S/N, estimates of stellar parameters have been derived using a χ^2 minimization technique (Zwitter et al. 2008; Siebert et al. 2011).

Using these data, Williams et al. (2011) identified a co-moving group of nearby ($0.5 \lesssim d \lesssim 10$ kpc) stars in the vicinity of the Aquarius constellation $(l, b) = (60^\circ, -55^\circ)$. Thus, the co-moving group was named the Aquarius stream. The stream is most apparent when examining velocities against galactic latitude for stars within $-70^\circ < b < -50^\circ$. Williams et al. (2011) employed a selection criteria of $-250 < V_{HEL} < -150$ km s^{-1}, $30^\circ < l < 75^\circ$ and $J > 10.3$ to maximize the contrast between the stream and background, identifying 15 candidates in the process. The average heliocentric velocity of these members was found to be $V_{HEL} = -199$ km s^{-1}, with a dispersion of 27 km s^{-1}. The radial velocities outputted by the RAVE survey are described to be ~ 2 km s^{-1}, so the wide kinematic distribution appears to be real.

Upon examining the galactic longitude and velocities of Aquarius stars, the stream appears quite distinct from the halo. In order to quantify the statistical likelihood that the Aquarius stream is truly distinct from the halo, Williams et al. (2011) compared the number of observed RAVE stars within $-70^\circ < b < -50^\circ$ against the Galaxia (Sharma et al. 2011) and Besançon (Robin et al. 2003) galaxy simulations. The predicted particles in each model between $-70^\circ < b < -50^\circ$ were binned in $\Delta l \times \Delta V_{hel}$ using varying grid cell sizes between $25 - 70^\circ$ and 20-100 km s^{-1} respectively. The RAVE sample was binned in the same way, and the statistical significance of the over-density is calculated for each cell. Williams et al. (2011) found the stream to be statistically significant (>4-σ) in 96% of the grid cell sizes employed for the Besançon model. By sampling the Galaxia model multiple times with varying extinction rates, a similar result was found: between 75 ± 15 % to 80 ± 18 % of grid cells showed the Aquarius stream to significant at the 4-

[1] This paper includes data gathered with the 6.5 meter Magellan Telescopes located at Las Campanas Observatory, Chile.

[2] Research School of Astronomy & Astrophysics, Australian National University, Mount Stromlo Observatory, via Cotter Rd, Weston, ACT 2611, Australia; acasey@mso.anu.edu.au
[3] Massachusetts Institute of Technology, Kavli Institute for Astrophysics and Space Research, 77 Massachusetts Avenue, Cambridge, MA 02139, USA

σ level or higher. Given the high-latitude and proximity of the stream, it is not surprising that dust had a negligible effect on the statistical significance. Williams et al. (2011) concluded that the over-density in l, V_{hel} is a true substructure, and neither the choice of galaxy model, cell size, nor the extinction model made any real difference to the stream detection significance.

Given the extent of stellar debris the Sagittarius dwarf has littered throughout the Milky Way, it is reasonable to suspect the Aquarius stream might originate from the Sagittarius dwarf. Indeed, the Aquarius stream stars do not lie far from the orbital plane of Sagittarius and the metallicities reported by Williams et al. (2011) are not dissimilar from the Sagittarius stream. However, Williams et al. (2011) found the Aquarius space positions and kinematics (specifically V_Z and V_ϕ) are quite distinct from Sagittarius. Based on the phase space information available, Williams et al. (2011) concluded that the newly discovered stream could not be positively associated with the Monoceros stream, Hercules-Aquila cloud, or either the Canis Major or Virgo over-densities.

The Aquarius stream has a metallicity of [Fe/H] ~ -1.0 (Williams et al. 2011), slightly more metal-rich than halo stars at the same distance. The dispersion in the stream's metallicity has yet to be fully characterised. Williams et al. (2011) found the stream to have an average of [M/H] $= -1.0 \pm 0.4$, compared to [M/H] $= -1.1 \pm 0.6$ for background stars after the same selection cuts had been employed. Of the 12 Aquarius stars in the Williams et al. (2011) discovery sample with stellar parameters, the metallicity range is wide: between –2.02 and –0.33 dex. Spectroscopic observations of high resolution with high signal-to-noise (S/N) are necessary to accurately determine the metallicity distribution.

To this end, Wylie-de Boer et al. (2012) obtained high-resolution ($R = 25,000$) spectra with modest S/N ($\sim$30 pixel^{-1}) for six Aquarius stream stars. Their data indicate a very narrow metallicity distribution: [Fe/H] $= -1.09 \pm 0.10$ dex extending between [Fe/H] $= -1.25$ to -0.98 dex. The largest [Fe/H] discrepancy between the two studies was Δ[Fe/H] $= -0.66$ dex for the most metal-rich star in the Williams et al. (2011) sample. The most metal-poor star in the Williams et al. (2011) study was not observed by Wylie-de Boer et al. (2012). The negligible level of chemical scatter observed in the Wylie-de Boer et al. (2012) sample is typical of what is found in globular or open clusters.

In addition to ascertaining stellar parameters, Wylie-de Boer et al. (2012) measured light element abundances for the Aquarius stream stars – the only study to do so until now. Their study primarily focussed on light elemental abundances: Na, O, Ni, Mg, and Al. Chemical patterns in these light elements arise as natural consequences of nucleosynthetic processes in massive stars. Thus, by observing the abundances of light elements in stars that formed together, we can infer the star-formation history and environment. More specifically, an anti-correlation in sodium and oxygen abundance has been identified in all well-studied globular clusters to date. Originally this was thought to arise from internal mixing along the giant branch. However, dwarf stars were found to exhibit strong Na-enhancement and O-depletions, contrary to what would be expected if the Na-O anti-correlation was purely a result of internal mixing. It is well known now that photospheric abundance variations resulting from internal mixing are limited to C, N and Li. While the exact astrophysical mechanism for oxygen-depletion remains under debate, the chemical relationship is well-established empirically. The Na-O pattern provides the best chemical evidence that their chemical enrichment history has been dominated by Sn II events and that those stars formed in a globular cluster-like environment.

From high-resolution spectroscopy of five stars in Aquarius, four of which had Na and O measurements, Wylie-de Boer et al. (2012) found two stars with super-solar sodium; slightly higher [Na/Fe] ratios than halo stars of the same metallicity. However, no strong oxygen depletion was evident in their data.

There are other chemical abundance patterns that allow us to infer the chemical evolution of a given cluster. Nissen & Schuster (1997) first noted that distant solar neighbourhood stars were enriched in [Ni/Fe] and [Na/Fe]. Fulbright (2000) came to a similar conclusion: only somewhat distant ($R_\odot > 20$ kpc) stars are likely to be sodium deficient. If the stellar halo has been built up from the accretion of smaller dwarf satellites, Nissen & Schuster (1997) proposed that this chemical trend may be indicative of the halo merger history since stars at larger $R_\odot$ are more likely to have been accreted rather than formed in-situ. Wylie-de Boer et al. (2012) found all the Aquarius stars in their sample to be enriched in both sodium and nickel; contrary to what would be expected if the stars originated from a disrupted dSph satellite. This provided an additional indication that the Aquarius stream stars originated in a globular cluster-like environment.

Combined with the low level of chemical scatter present in their sample, these chemical indicators led Wylie-de Boer et al. (2012) to conclude that the Aquarius stream must be the result of a tidally disrupted globular cluster. Williams et al. (2011) had previously precluded this possibility with any known globular clusters after modelling an Aquarius-like progenitor infalling onto the Milky Way and comparing the predicted l, b, V_{hel} with known, nearby globular clusters of similar metallicities. No known globular cluster could match their simulation.

We seek to investigate the nature of the Aquarius stream, specifically the recent globular cluster origin claim made by Wylie-de Boer et al. (2012). We present a detailed analysis for five Aquarius stream members from high-resolution, high S/N observations taken using the Magellan Inamori Kyocera Echelle spectrograph (Bernstein et al. 2003) on the Magellan Clay telescope. Details of the observations and data reduction are outlined in the following section. The data analysis is chronicalled in Section 3 and a detailed discussion of these results resides in Section **??**. In Section **??** we present our conclusions and critical interpretations.

2. OBSERVATIONS & DATA REDUCTION

The most complete sample of Aquarius stream stars is presented in the discovery paper of Williams et al. (2011). Our sample includes five stars: four common to the Wylie-de Boer et al. (2012) study, and an additional star from the original Williams et al. (2011) sample. The additional candidate, J2306265-085103, was observed by

TABLE 1
OBSERVATIONS

Designation	α (J2000)	δ (J2000)	Observed Date	Airmass	Seeing (")	t_{exp} (secs)	S/N[a] (px^{-1})	V_{rad} (km s^{-1})	V_{hel} (km s^{-1})	V_{err} (km s^{-1})
C2225316-14437	22:25:31.7	−14:54:39.6	2011-07-30	1.033	...	...	135	–168.6	–156.4	0.1
C2306265-085103	23:06:26.6	−08:51:04.8	2011-07-30	1.096	...	...	100	–240.4	–221.1	0.1
HD41667	06:05:03.7	−32:59:36.8	2011-03-13	1.005	...	...	...	314.4	...	0.8
HD142948	16:00:01.6	−53:51:04.1	2011-03-14	1.107	...	...	...	6.8	...	0.4
J221821-183424	22:18:21.2	−18:34:28.3	2011-07-30	1.026	...	...	115	–170.2	–159.5	0.1
J223504-152834	22:35:04.5	−15:28:34.9	2011-07-30	1.047	...	...	135	–179.0	–169.7	0.1
J223811-104126	22:38:11.6	−10:41:29.4	2011-07-30	1.218	...	...	115	–250.1	–235.7	0.1

[a] S/N measured at 6000 Å for each target.

the RAVE survey but had a S/N ratio too low for stellar parameters to be accurately determined. All program stars were observed in July 2011 in good seeing at low airmass (Table 1), and X additional standard stars were observed in March 2011. All observations were taken using a 1.0" slit, providing a spectral resolution of $R = 28,000$ in the blue and $R = XX,XXX$ in the red arm. The total exposure times for our program stars varied per star from X-Y seconds to ensure a Signal-to-Noise ratio (S/N) in excess of 100 per pixel element at 600 nm.

Calibration frames were taken at the start of each night, including twenty flat-field frames (10 quartz, 10 milky) and 10 Th-Ar arc lamp exposures for wavelength calibration. The data were reduced using the CarPy pipeline[4]. One of our standard stars, HD 41667, was also reduced using standard extraction and calibration methods in IRAF. The resultant spectra from both reduction approaches were compared for residual fringing, S/N, and wavelength calibration. No noteworthy differences were present, and thus the CarPy pipeline was utilized for the remainder of the reductions. Each reduced echelle order was carefully normalized using a third order spline. Normalized orders were stitched together to provide a single one-dimensional spectrum from 3800-9400 Å.

The white dwarf HR 6141 was observed on X with a S/N of 400 pixel^{-1} as a telluric standard. The S/N ratio for HR 6141 exceeds the S/N ratio in any of our program stars. Although the atmospheric conditions at Las Campanas Observatory are certain to change throughout the night and between observing runs, we are primarily using this spectra to identify lines that are affected by telluric absorption. Critical transitions necessary for abundance analyses that are affected by the earth's atmosphere are corrected for telluric absorption (see §**??**).

3. ANALYSIS

3.1. *Radial Velocities*

The radial velocity for each star was determined in a two-step method. An initial estimate of the radial velocity was ascertained by cross-correlation with a synthetic spectrum of a giant star with $T_{eff} = 4500\,$K, $\log g = 1.5$, and [M/H] $= -1.0$ across the wavelength range $8450-8700$ Å. The observed spectrum was shifted to the pseudo-rest frame using this initial velocity estimate. Velocities found from cross-correlation are typically within $1\,\mathrm{km\,s^{-1}}$ of our final published value.

With our spectra at near-rest, we measured the equivalent widths of ∼200 lines by automatically fitting Gaussian functions to the absorption profiles (see Section 3.2). Fitted Gaussian profiles provide us with a measured equivalent width, the full-width half-maximum and the central wavelength of the profile. Thus, the residual radial velocity can be found from the ratio of the central and rest line wavelengths. The final radial velocity for the star is provided by the initial velocity and the mean of ∼200 residual line velocity measurements. Figure 1 shows the line velocities for HD41667 after being placed at pseudo-rest using our cross-correlation velocity of 314.4 km s^{-1}. As expected, the mean residual offset is small (-0.75 km s^{-1}), and the standard deviation is 0.79 km s^{-1} from 164 line measurements. This provides us with a final measured radial velocity of 313.7 ± 0.1 km s^{-1}. This process was performed for all observations. The radial velocities published in Table 1 are the final values from this two-step method. Heliocentric velocities agree quite well with the Williams et al. (2011) published values: the mean absolute offset is $\langle \Delta V_{hel} \rangle = 2.8\,\mathrm{km\,s^{-1}}$, demonstrating the accuracy of the velocities published by the RAVE survey.

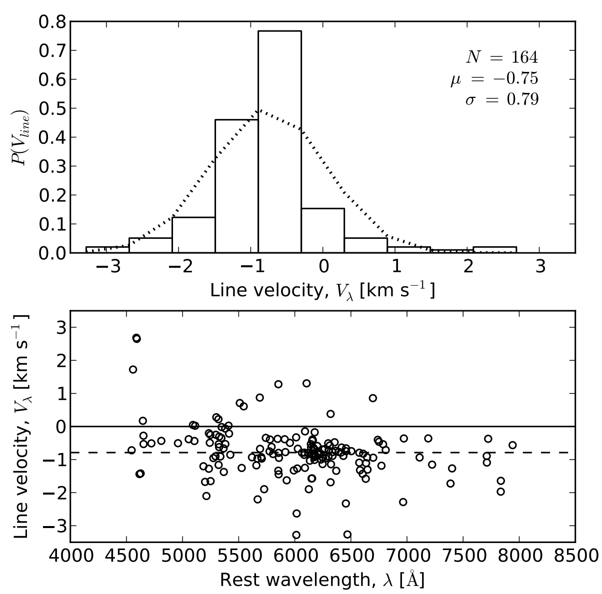

FIG. 1.— Residual velocities for each absorption line with a well-fitted Gaussian profile after correcting for doppler shift with our initial cross-correlation measurement. The mean residual velocity $-0.75\,\mathrm{km\,s^{-1}}$ is within the 1-σ cross-correlation uncertainty of $\pm 0.9\,\mathrm{km\,s^{-1}}$.

[4] http://code.obs.carnegiescience.edu/mike

3.2. *Line Measurements*

For the measurement of atomic absorption lines, we employed the line list of Yong et al. (2005) with additional transitions of Cr, Sc, Zn, and Sr from Frebel et al. (2010). The line list was augmented with hyperfine-structure data for Sc and Mn from the Kurucz compilation **?**. Molecular line data for CH was taken from **??**. For lines with hyperfine structure, blended transitions or molecular features, we determined the abundance using a spectral synthesis approach. For all other transitions, equivalent widths were measured to determine the abundance.

The equivalent widths for all absorption lines were measured automatically using software written for this study. Given the rest wavelength and an initial guess of the full-width half-maxium (FWHM), a Gaussian function is iteratively fitted to the absorption profile. At the same time, the local continuum is found within 20 Å either side of the rest wavelength using a second-order polynomial. Measuring the local continuum ensures any errors in our initial normalisation or order-stitching do not propagate through to our equivalent width measurements. When determining the local continua, any neighbouring group of pixels that deviate significantly (>2-σ) from the local continua either belong to a persistent cosmic ray hit, or they are trough points of a neighbouring absorption profile. We attempt to fit a Gaussian profile to each group of deviating pixels, using the current best estimate for the local continuum. If a Gaussian profile is successfully fitted to the deviating group and its surrounding pixels, we assume the outlier points belong to an absorption profile and all points belonging to that profile are excluded from the continuum determination.

When fitting Gaussian profiles, the χ^2 difference between the observed spectra and the fitted profile is minimized. In order to account for crowded absorption regions, where the χ^2 value might be influenced by a nearby profile, our χ^2 function is weighted based on the distance to the rest wavelength by the function

$$W_{\lambda_i} = 1 + \exp\left(\frac{-(\lambda_i - \lambda_r)^2}{4\sigma^2}\right) \tag{1}$$

where the rest wavelength (λ_r) and FWHM (σ) are free parameters in the iterative fitting process. As a consequence of Eq. 1, pixels near the rest wavelength are weighted higher than those on the wings, forcing the fitting scheme to disregard blended or crowded regions. Although this approach relies on a reasonably accurate radial velocity correction (<4 km s^{-1}; which is easily achieved), it greatly improves the accuracy and robustness of the equivalent width measurements.

The results of our iterative Gaussian fitting approach are completely *insensitive* to the initial FWHM guess. Increasing the initial FWHM estimate from 0.1 Å to 1 or 2 Å – which are unphysically large values for high-resolution spectra – does not alter either the FWHM or the equivalent width for any of our measurements. Only a small increase in computational cost is observed. Although we are extremely confident in our automatic equivalent width measurements, every absorption profile was examined by eye for quality, and spurious measurements were excluded.

We list the atomic data and measured equivalent widths for atomic lines used during this analysis in Table **??**. Saturated lines were excluded by removing measurements with reduced equivalent widths, $\log_{10}(EW/\lambda) > -4.5$ dex. A minimum detectable equivalent width was calculated as a function of wavelength based on the S/N, and only lines that exceeded a 3-σ detection significance were included. We have verified the approach by comparing our measurements of 156 lines in HD 140283 with the study of Norris et al. (1996). We only included measurements in the Norris et al. (1996) study that were not marked with line quality parameters. Excellent agreement is found between the two studies, which is illustrated in Figure 2. The mean difference is a negligible 0.64 ± 2.78 mÅ, and no systematic trend is present. We note that the scatter may be directly attributed to the observed S/N, as other studies using the same equivalent width measurement software described here find better agreement with hand measurements for spectra with higher S/N (0.20 ± 0.16 mÅ with $S/N \sim X$, 0.25 ± 0.28 mÅ with $S/N \sim Y$; **?**).

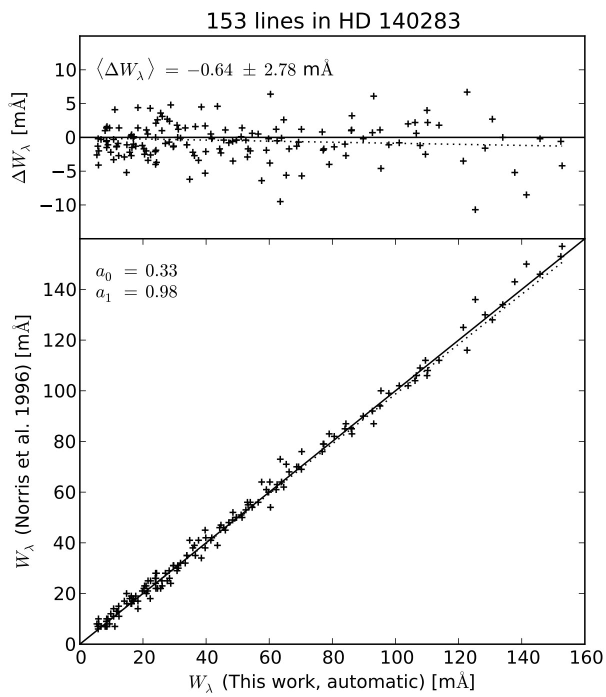

Fig. 2.— A comparison showing equivalent widths measured for HD 140283 using our automatic routine (see §3.2), and those found by careful hand measurements in Norris et al. (1996). No systematic trend is present, and the mean difference between these studies is $\langle \Delta W_\lambda \rangle = -0.64 \pm 2.78$ mÅ.

TABLE 2
List of Line Transitions and Equivalent Width Measurements

				Equivalent Width				
Wavelength (Å)	Transition	LEP (eV)	log gf	C2225316-14437 (mÅ)	C2306265-085103 (mÅ)	J221821-183424 (mÅ)	J223504-152834 (mÅ)	J223811-104126 (mÅ)
6300.300	8.0	0.00	–9.717	45.37	66.93	38.48	32.85	17.87
6363.780	8.0	0.02	–10.185	19.47	28.31	12.96	18.83	···
5688.190	11.0	2.11	–0.420	···	···	48.97	131.49	38.41
6154.230	11.0	2.10	–1.530	24.06	38.89	···	48.49	···
6160.750	11.0	2.10	–1.230	37.72	58.49	···	65.72	···
6318.720	12.0	5.11	–1.970	···	47.94	14.69	62.79	8.88
6319.240	12.0	5.11	–2.220	30.84	···	5.51	···	···
6965.410	12.0	5.75	–1.510	···	···	···	59.22	···
7387.690	12.0	5.75	–0.870	51.71	56.30	24.68	76.01	23.99
6696.020	13.0	3.14	–1.340	72.83	63.60	12.99	···	···
6698.670	13.0	3.14	–1.640	39.67	33.44	···	39.50	···
7835.310	13.0	4.02	–0.470	47.77	38.44	···	55.91	5.39
7836.130	13.0	4.02	–0.310	62.78	44.72	···	69.13	13.23
5690.430	14.0	4.93	–1.751	56.17	43.76	25.75	53.45	16.77
5793.070	14.0	4.93	–1.843	46.13	39.81	19.33	48.39	···
6125.020	14.0	5.61	–1.506	40.93	23.45	10.86	34.74	···
6145.010	14.0	5.62	–1.362	33.93	21.66	16.11	32.75	10.02
6155.130	14.0	5.62	–0.786	67.36	53.11	35.29	72.00	24.98
6166.440	20.0	2.52	–1.142	94.19	105.46	42.32	99.45	35.88
6169.040	20.0	2.52	–0.797	112.06	120.91	66.31	120.48	55.48
6169.560	20.0	2.53	–0.478	127.89	141.16	83.69	136.37	71.35
6455.600	20.0	2.52	–1.290	80.79	91.41	31.35	89.20	25.98
5526.820	21.1	1.77	0.130	98.84	113.34	100.84	98.40	51.08
5657.880	21.1	1.51	–0.500	96.46	107.49	92.74	95.42	41.21
5667.150	21.1	1.50	–1.240	59.41	75.04	45.00	58.54	14.51
5669.040	21.1	1.50	–1.120	···	92.51	57.27	75.19	18.20
6245.610	21.1	1.51	–0.980	67.12	83.60	53.34	67.38	14.75
6604.600	21.1	1.36	–1.480	65.58	82.06	49.37	65.92	17.81
6064.630	22.0	1.05	–1.888	59.69	80.86	···	58.58	···
6091.170	22.0	2.27	–0.367	45.15	59.09	···	56.28	···
6312.240	22.0	1.46	–1.496	46.16	63.41	···	48.78	···
6336.100	22.0	1.44	–1.687	35.88	54.10	···	42.33	···
5154.080	22.1	1.57	–1.920	112.25	···	114.05	···	53.89
5185.910	22.1	1.89	–1.350	···	101.45	105.46	···	55.30
5336.790	22.1	1.58	–1.690	116.30	124.58	119.55	103.98	61.40
5381.030	22.1	1.59	–2.080	···	131.44	101.94	109.93	47.96
5727.060	23.0	1.08	–0.010	122.36	···	26.00	116.79	9.13
6090.220	23.0	1.08	–0.060	93.58	115.58	23.62	92.84	···
6216.360	23.0	0.28	–1.290	108.80	···	16.92	109.33	···
6251.820	23.0	0.29	–1.340	94.66	124.37	···	92.43	···
6274.640	23.0	0.27	–1.670	65.49	93.82	···	61.51	···
6504.160	23.0	1.18	–1.230	22.95	33.69	···	31.93	···
4545.950	24.0	0.94	–1.370	···	···	80.22	···	···
4580.056	24.0	0.94	–1.650	···	···	···	···	44.22
4616.137	24.0	0.98	–1.190	128.75	139.25	89.37	126.24	59.88
4626.188	24.0	0.97	–1.320	122.24	136.41	82.24	···	56.90
4646.150	24.0	1.03	–0.740	···	···	110.65	146.08	75.35
4651.280	24.0	0.98	–1.460	127.78	140.58	75.40	116.31	48.44
4652.158	24.0	1.00	–1.030	138.48	···	96.92	138.00	66.74
5206.040	24.0	0.94	0.020	···	···	···	···	132.81
5247.564	24.0	0.96	–1.640	141.39	···	76.09	···	46.66
5296.690	24.0	0.98	–1.360	149.87	···	85.01	140.97	59.00
5300.740	24.0	0.98	–2.000	120.48	···	···	112.22	···
5345.800	24.0	1.00	–0.950	···	···	115.38	···	81.14
5348.310	24.0	1.00	–1.210	150.80	···	94.76	142.37	63.02
5409.770	24.0	1.03	–0.670	···	···	132.36	···	92.13
4558.594	24.1	4.07	–0.656	···	···	···	101.77	46.52
4588.142	24.1	4.07	–0.826	46.04	52.99	60.53	55.00	35.95
4591.992	24.1	4.07	–1.419	···	···	29.08	28.53	19.56
6013.530	25.0	3.07	–0.251	89.19	114.55	22.18	109.41	14.81
6016.670	25.0	3.08	–0.100	93.98	116.01	28.15	113.02	17.06
6021.800	25.0	3.08	0.034	97.50	116.02	39.08	110.74	19.90
5044.210	26.0	2.85	–2.034	···	···	···	···	33.70
5054.640	26.0	3.64	–1.938	37.96	···	···	···	···
5242.490	26.0	3.63	–0.980	94.34	101.83	72.92	···	49.25
5321.110	26.0	4.43	–1.106	34.97	35.32	11.14	···	···
5322.040	26.0	2.28	–2.840	93.10	103.03	59.48	···	30.88
5326.140	26.0	3.57	–2.130	40.39	51.67	13.75	48.44	···
5365.400	26.0	3.57	–1.040	···	100.31	···	93.75	···
5367.480	26.0	4.41	0.430	108.42	118.03	92.35	119.08	73.73
5379.570	26.0	3.69	–1.530	71.36	81.40	34.91	75.65	19.57
5491.840	26.0	4.18	–2.250	···	···	···	17.29	···
5618.630	26.0	4.21	–1.292	43.46	54.27	20.25	57.44	11.30
5701.550	26.0	2.56	–2.216	118.51	134.78	91.77	119.47	49.50
5705.470	26.0	4.30	–1.420	29.24	41.47	10.92	44.49	7.70
5741.850	26.0	4.25	–1.689	36.19	37.02	13.01	48.22	···
5775.080	26.0	4.22	–1.310	54.96	62.12	25.34	67.38	14.67
5778.450	26.0	2.59	–3.480	42.75	55.83	13.43	50.14	···

3.3. *Model Atmospheres*

We have employed the ATLAS9 plane-parallel stellar atmospheres of Castelli & Kurucz (2003). These one-dimensional models ignore any centre-to-limb spatial variations, assume hydrostatic equilibrium and no convective overshoot from the photosphere. The stellar parameter spacing between models is 250 K, 0.5 dex in surface gravity, 0.5 dex in [M/H] and 0.1 dex in [α/Fe]. We interpolated the atmospheric pressures, densities, temperatures, and opacities between stellar atmosphere models using the Quickhull algorithm (Barber et al. 1996). Quickhull is reliant on Delaunay tessellation, which suffers from extremely skewed cells when the grid points vary in size by orders of magnitude – as T_{eff} values do compared to $\log g$ or [X/H]. If unaccounted for, performing interpolation using these asymmetric cells can manifest as significant errors in atmospheric properties across all photospheric depths. We scaled each stellar parameter between zero and unity prior to interpolation in order to minimise these errors. During this step, $\log g$, [M/H] and [α/Fe] points were scaled such that we simultaneously interpolate linearly in T_{eff} and logarithmically in all other parameters.

3.4. *Stellar Parameters*

The most recent version of the spectral synthesis code MOOG (Sneden 1973) has been used to derive individual line abundances and stellar parameters. This version of MOOG employs Rayleigh scattering (Sobeck et al. 2011) instead of treating scattering as true absorption, which is particularly important for transitions blue-ward of 450 nm. This is noteworthy, but is less relevant for this analysis as most of our line measurements are red-ward of 450 nm. Absorption lines are assumed to form under the assumption of local thermal equilibrium.

3.4.1. *Effective Temperature*

The effective temperature for each star was found by demanding a zero-trend in excitation potential and abundance for each measured Fe I line. In the same way, the microturbulence was found by demanding a zero trend in reduced equivalent width against abundance. Linear relationships with slopes of $|0.001|$ dex were considered to be converged.

3.4.2. *Photometric Effective Temperatures*

The effective temperatures published for all of our stars in Table **??** have been derived spectroscopically (see §**??**). As a consistency check for our spectroscopic temperatures, we have also estimated effective temperatures using infrared photometry from the 2MASS catalog. The $J-K$ colour has been employed for these calculations because it has the least dependence on metallicity.

The Aquarius stream is relatively close and at high-latitude, so significant extinction by dust is not expected. The dust maps of Schlegel et al. (1998) estimate that the extinction for our stars varies between E(B-V) = 0.03 to 0.07 mags. However, these maps are not perfect. As an alternative to using the Schlegel et al. (1998) dust maps, the level of extinction towards a star can be found by the strength of their interstellar Na D or K I lines (Munari & Zwitter 1997). The interstellar lines must be sufficiently separated from the stellar lines in order for the extinction to be measurable. Unfortunately this was the case in only one of our stars, J223811. We measure the equivalent width of the Na D I line in J223811 to be 302.4 mÅ, which corresponds to an E(B-V) = $0.12^{+0.01}_{-0.02}$ according to the Munari & Zwitter (1997) relationship. This is a significantly higher value than what the Schlegel et al. (1998) dust map value of E(B-V) = 0.07 for J223811. Both extinction values have been used to calculate photometric temperatures.

Although all of our targets are giant stars, two different T_{eff}-colour relationships have been employed: the Alonso et al. (1999) calibration for giants, and the Casagrande et al. (2010) calibration for dwarfs and subgiants. All photometrically-derived temperatures are listed in **??**. The Alonso et al. (1999) $J-K$ scale is insensitive to metallicity effects, and is in good agreement with our spectroscopic temperatures. For the Casagrande et al. (2010) $J-K$ relationship, which has a slight metallicity dependency, we have utilized the spectroscopically-derived [Fe/H] values shown in Table **??**.

The effective temperatures that we have found from spectroscopy agree fairly well with the photometric temperature estimates. For three of our stars, the temperatures we find are in between the two color-temperature relationships. There are two noteworthy deviations though: J223504-152834 and J223811-104126. For J223504-152834 we find the star to have an effective temperature of 4620 K, 40 K hotter than the Casagrande et al. (2010) dwarf/sub-giant relationship, and ~500 K hotter than the Alonso et al. (1999) temperature. Our temperature of 4620 K is in good agreement with previous spectroscopic determinations (4795 K; Williams et al. (2011), 4597 K; Wylie-de Boer et al. (2012)). The fact that the Alonso et al. (1999) photometric temperature relationship for giants predicts a temperature that is ~500 K cooler than the spectroscopically-derived values may be attributed to an underestimated amount of dust towards J223504-152834. A higher than expected level of extinction along the line-of-sight would produce cooler temperatures than the true effective temperature.

The F-giant J223811-104126 has two extinction values available: the Schlegel et al. (1998) value of $E(B-V) = 0.07$ and the 0.12 value that we have determined from the interstellar Na D1 line. Given the inherent difficulties in producing dust maps, and the known problems associated with them, we believe the $E(B-V) = 0.12$ determination to be more accurate. However, using the Schlegel et al. (1998) extinction with the Alonso et al. (1999) color-temperature relationship yields excellent agreement (within 6 K) with our spectroscopic temperatures. Employing our more accurate reddening determination yields 5215 K, within the uncertainties of the relationship. The Casagrande et al. (2010) scale is ~250 K hotter in both cases.

Thus, with the exception of J223504-152834, the Alonso et al. (1999) giant relationship agrees well (±100 K) with our spectroscopically derived values. The Casagrande et al. (2010) relationship is also in relatively good agreement with our spectroscopic temperatures, although we note that this relation was derived primarily for dwarfs/sub-giants. The discrepancy in J223504-152834 could very well be due to under-estimated redden-

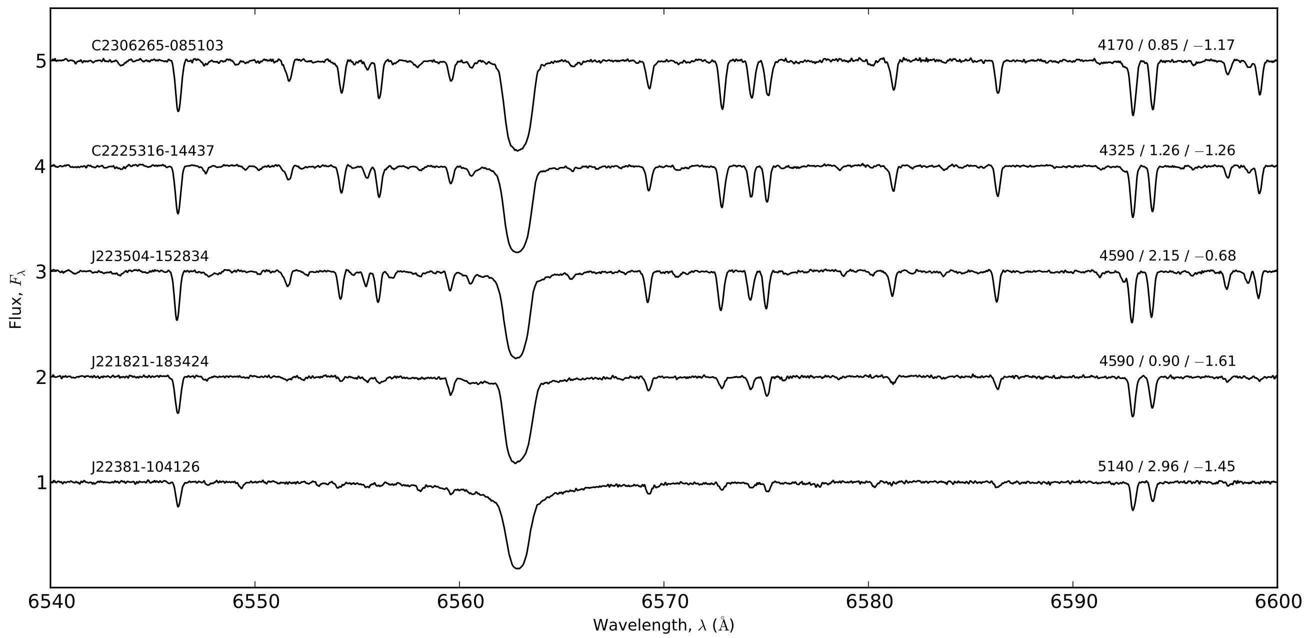

Fig. 3.— Spectra for all Aquarius stream stars.

TABLE 3
Reddening & Photometric Temperatures

Designation	E($B-V$) (mag)	$(J-K)_0$	T_{phot} Alonso (K)	T_{phot} Casagrande (K)
C222531-144370	0.03	0.75	4247	4391
C230626-085103	0.05	0.82	4091	4200
J221821-183424	0.03	0.64	4546	4747
J223504-152834	0.04	0.69	4110	4579
J223811-104126	0.07	0.48	5104	5367
	0.12[a]	0.45	5215	5484

[a]Extinction derived from interstellar Na D1 line (see 3.4.2)

ning along the line-of-sight. An extinction of $E(B-V) = 0.10$ would be required for the Alonso et al. (1999) relation to yield a temperature of $\sim$4500 K, within the uncertainties of our effective temperature derived from spectroscopy. Such a discrepancy in extinction is large, but not unheard of (e.g., the case of J223811-104126 or see **?**). Although we suspect J223504-152834 to have a higher reddening than $E(B-V) = 0.04$, we have adopted the Schlegel et al. (1998) value for this analysis.

3.4.3. *Surface Gravity*

Surface gravity was found by forcing the mean Fe I and Fe II abundances to be equal, whilst maintaining zero trends with the excitation potential, reduced equivalent width and abundance. After these parameters had converged, the model metallicity was exactly matched to that of our line abundances. Line abundances that were unusually deviant (3σ) from the mean were removed. The largest number of outlier measurements removed for any observation was nine for C222531-144370.

3.4.4. *Metallicity, [M/H]*

Determining the stellar parameters for a given star is an iterative process. Once the effective temperature, microturbulence and surface gravity were deduced, the model atmosphere abundance was matched to our solar-scaled Fe I abundance. The degeneracy between parameters required a refinement of the stellar parameters until the line abundances were consistent with the model atmosphere.

3.5. *Abundances*

We have scaled our abundances to solar values using the chemical composition of Asplund et al. (2009).

3.5.1. *Carbon*

3.5.2. *Oxygen*

Oxygen is a particularly difficult element to measure. There are only a handful of lines available in an optical spectrum: the forbidden [O I] lines at 630 nm and 636 nm, and the O I triplet lines at 777 nm. The forbidden lines are very weak, and become immeasurable in either hot and/or metal-poor stars ([Fe/H] $\lesssim -1.5$ dex). When they are present, depending on the radial velocity of the star, the [O I] can be significantly affected by telluric absorption. Moreover, the 630 nm line is blended with a Ni I absorption line (Allende Prieto et al. 2001), and hence the region requires careful consideration. Although the O I triplet lines at 777 nm are stronger than the forbidden lines, they are extremely susceptible to NLTE and 3D effects (**?**), and sensitive to changes in microturbulence. García Pérez et al. (2006) showed that oxygen abundances measured under the assumption of LTE in their sample are 0.08 dex higher than abundances derived from the 'true' oxygen content derived from the forbidden lines (García Pérez et al. 2006).

The [O I] lines were measurable in four of our candidates. Careful consideration was taken when correcting for telluric absorption, and we inspected all lines for any contamination by the earth's atmosphere. The 6300λ line in one of our candidates, C2306265-085103, was suf-

TABLE 4
Stellar Parameters

Designation	T_{eff} (K)	$\log g$ (dex)	v_t ($\mathrm{km\,s^{-1}}$)	[Fe/H] (dex)	T_{eff} (K)	$\log g$ (dex)	v_t ($\mathrm{km\,s^{-1}}$)	[Fe/H] (dex)	Source
Standard Stars									
HD41667	4630	1.70	1.66	–1.21	4605	1.88	1.44	–1.16	Gratton et al. (2000)
HD44007	4790	1.78	1.63	–1.80	4850	2.00	2.20	–1.71	Fulbright (2000)
HD142948	4950	2.19	1.78	–0.79	4713	2.17	1.38	–0.77	Gratton et al. (2000)
Program Stars									
C2225316-14437	4325	1.26	1.78	–1.26	4235 ± 118	1.45 ± 0.21	1.96 ± 0.11	-1.20 ± 0.14	Wylie-de Boer et al. (2012)
C2306265-085103	4170	0.85	1.81	–1.17	...	...	...	...	...
J221821-183424	4590	0.90	1.91	–1.61	4395 ± 205	1.45 ± 0.35	1.96 ± 0.18	-1.15 ± 0.21	Wylie-de Boer et al. (2012)
J223504-152834	4590	2.15	1.45	–0.68	4597 ± 158	2.40 ± 0.14	1.47 ± 0.07	-0.98 ± 0.17	Wylie-de Boer et al. (2012)
J223811-104126	5140	2.96	1.33	–1.45	5646 ± 147	4.60 ± 0.15	1.09 ± 0.11	-1.20 ± 0.20	Wylie-de Boer et al. (2012)

ficiently affected by telluric absorption such that we considered the line immeasurable. Thus, only the 6363λ line was used to derive an oxygen abundance for C2306265-085103. In our hottest star, J223811-104126, the forbidden oxygen lines were not detected above a $3-\sigma$ significance. After synthesising the region, we deduce a conservative upper limit of $[\mathrm{O/Fe}] < -0.50$ dex from the [O I] lines. This is consistent with the rest of our candidates, with [O/Fe] abundances varying between 0.41 to 0.57 dex.

In order to derive an oxygen measurement for J223811-104126, we were forced to use the triplet lines at 777 nm. Each line was synthesised, and a mean abundance was calculated for each candidate. Abundances determined from the oxygen triplet lines were systematically +0.27 dex higher than found from the [O I] lines. García Pérez et al. (2006) found [O/Fe] values based on the O I permitted triplet lines are on average $+0.19 \pm 0.07$ dex higher than those found from the forbidden lines, after NLTE corrections of -0.08 dex had been applied. Thus, our 0.27 dex offset between measurements of the [O I] and O I triplet lines is exactly the same as found by García Pérez et al. (2006), which we attribute to a combination of NLTE, 3D and other systematic effects. García Pérez et al. (2006) concluded the weak forbidden lines, when not too weak, probably give the most reliable estimate of [O/Fe].

From the permitted O I triplet, we derive an oxygen abundance of $[\mathrm{O/Fe}] = 0.41 \pm 0.01$ dex (random scatter) for J223811-104126. This measurement will be systematically higher than the 'true' abundance if it were discernible from the [O I] lines, on the order of ~ 0.27 dex. When we apply this crude offset derived from the rest of our sample, we arrive at a corrected abundance of $[O/Fe] = 0.14 \pm 0.08$ dex for J223811-104126. This is the most oxygen-deficient star in our sample.

3.5.3. *Sodium*

Sodium is mainly produced through through carbon burning in massive stars by the dominant $^{12}\mathrm{C}(^{12}\mathrm{C},p)^{23}\mathrm{Na}$ process. The final Na abundance is dependent on the neutron excess of the star, which slowly increases during carbon burning due to weak interactions (**?**). Massive stars ($> 8M_\odot$) eventually deliver their manufactured sodium to the interstellar-medium through SN II events. Because the eventual SN II explosion is devoid of any significant beta-decay processes, the neutron excess of the exploded material is representative of the pre-explosion abundance.

The explosive material eventually condenses to form the next generation of stars, which will have a net increase in their neutron excess with respect to when their predecessors formed. Since the Na-production rate is correlated with the neutron excess, an overall increase in the total Na and Na-production rate between stellar generations is expected. Thus, an increase in the Na abundance between generations of massive stars is a natural consequence of nucleosynthesis. Sodium content also becomes important for production of Ni during the SN II event (see §**??**) because ^{23}Na is the only stable isotope produced in significant quantities during the C- (or O-) burning stages. A small fraction of ^{22}Na is also forged through proton capture on ^{21}Ne in the carbon shell, an effect which is enhanced by neutrinos spallating abundant elements like ^{16}O and ^{20}Ne, making free protons available for capture (Woosley & Weaver 1995).

3.5.4. *α-elements (Mg, Ca, Si and Ti)*

The α-elements (Mg, Ca, Si and Ti) are forged through α-particle capture in assorted burning stages of stellar evolution, including the burning of carbon, neon and silicon. Although Ti ($Z = 22$) is not formally an α-element, its abundance generally varies with those of the other α-elements and therefore has been included here.

Depending on the radial velocity of the star, some magnesium lines were be affected by telluric absorption, particularly the 6318λ and 6965.4λ lines. Atmospheric absorption was most notable for C2225316-14437, where three of the four Mg transitions in our line list suffered some degree of telluric absorption, requiring an attentive correction. Every amended absorption profile was carefully examined, and lines with suspicious profiles were excluded from the final magnesium abundance.

Of all the α-elements, calcium has the smallest measurement scatter in our stars. Four line measurements were used for each star, with a measurement uncertainty of 0.01 dex. As shown in Figure **??**, all Aquarius stars show super-solar Ca abundances, ranging between 0.23 to 0.43 dex, consistent with both [Mg/Fe] and [Si/Fe] measurements. However, C2225316-14437 has an unusually high silicon abundance ($[\mathrm{Si/Fe}] = 0.72$), well outside the uncertainties of the rest of our sample. C2225316-14437 does not demonstrate unusually high abundances of any other α-element, and the silicon lines are not af-

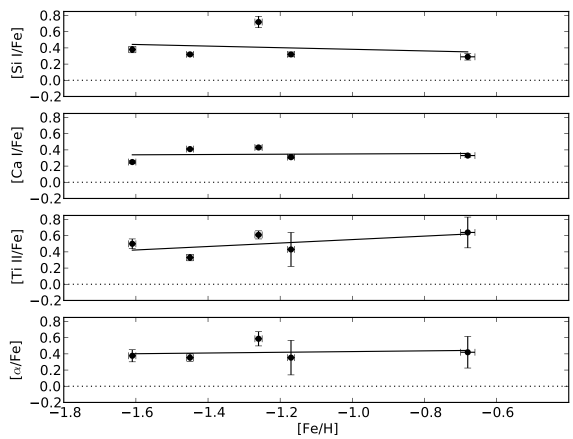

FIG. 4.— A plot showing [α/Fe] for all Aquarius stream stars.

fected by telluric absorption. Moreover, the Si lines are in relatively good agreement with one another. If we exclude the most prominent outlier, then the mean abundance drops only slightly to [Si/Fe] $= 0.70 \pm 0.04$ dex. The lowest silicon line abundance for C2225316-14437 is [Si/Fe] $= 0.57$ dex, still significantly higher than the averaged abundance for any other star.

3.5.5. *Aluminium*

There are six aluminium transition lines available in our optical spectra. The strongest of these lines occur at 3944 and 3961 Å, and are visible in all of our stars. However, this is a particularly crowded spectral region: these lines fall between the strong Ca H and K lines, with the 3961 Å transition clearly in the wing of the Ca H line. This makes the continuum determination and subsequent Al measurement non-trivial, especially given the metallicity of our stars. Instead, we have measured Al abundances from the other transitions available in our spectra: the Al I lines at 6696, 6698, 7835 and 7836 Å. Although these lines are weaker than the bluer Al I lines, their surrounding regions are uncrowded.

Generally the four Al I lines are in reasonable agreement with one another, yielding random scatter of less than 0.05 dex. However these lines were not always detected in the data. The strength of the lines is noticeably weakened below a 3-σ detection with decreasing metallicity and increasing temperature. For our most metal-poor star, J221821, only one Al I line was detectable, and so we have adopted an uncertainty of 0.10 dex.

3.5.6. *Iron-peak Elements (Sc, V, Cr and Mn)*

Scantium, Vanadium, Chromium and Manganese. All very vanilla, exhibiting a downward trend with [Fe/H]. Data.

3.5.7. *Barium*

Barium is a neutron-capture element, primarily produced through the *s*-process, but can be forged from a variety of nucleosynthetic processes. Measuring barium requires some careful consideration. The strong resonance lines at 4554 Å and 4934 Å have appreciable hyperfine splitting, which if unaccounted for can result in over-estimated abundances. There are a few singly ionized lines available in our spectra which do not suffer from strong hyperfine splitting, namely the 5853, 6141 and 6496 Å transitions. Depending on the radial velocity of the star, sometimes our 6496 Å line was affected by small amounts of telluric absorption. In these cases the line was discarded. The abundances tabulated in Table 5 are based on the remaining clean Ba II lines at 5853 and 6141 Å, which are generally in good agreement with each other, and the 6496 Å line where available.

Our standard stars have [Ba/Fe] abundances very typical of the Milky Way halo. Only one of our standard stars, HD 44007, has published [Ba/Fe] abundances from high-resolution spectra. We find HD 44007 to have [Ba/Fe] $= -0.05 \pm 0.04$, which is in between existing published measurements from Fulbright (2000) and Burris et al. (2000) of -0.27 and 0.05 dex, respectively.

With one exception, the Aquarius stream stars have barium abundances that are quite similar to the stellar halo, ranging between [Ba/Fe] $= -0.02$ to 0.15 dex. The exception is C2225316, which has an anomalously high barium abundance of [Ba/Fe] $= 0.68$ dex. This is $\sim$ 0.60 dex higher than the Milky Way trend at its given [Fe/H] $= -1.19$ dex. Our three Ba II lines in C2225316 are in excellent agreement: 0.67, 0.68, and 0.72 dex. The 6496 Å transition has negligible telluric contribution (e.g. Figure **??**), so it was included for this star. At least in Al, Si, Cr and Ba abundances (see sections **??**, 3.5.4, **??**), this star appears to be chemically distinct from the other Aquarius stream stars in our sample.

3.6. *Distances*

3.7. *Dynamics*

4. DISCUSSION

We seek to investigate the nature of the Aquarius stream, as well as the specific globular cluster origin claim made by Wylie-de Boer et al. (2012).

4.1. *Stellar Parameter Discrepancies with Wylie-de Boer et al. (2012)*

The stellar parameters reported in Wylie-de Boer et al. (2012) differ slightly to those found in Table **??**. Wylie-de Boer et al. (2012) deduce their stellar parameters by minimizing the χ^2 difference between the observed spectra, and spectra from the Munari et al. (2005) synthetic spectral library after it was convolved and re-sampled to match the observations. The comparison regions used for analysis were 4900-5200 Å and 5575-5725 Å. In general, temperatures between the two studies agree within the uncertainties, with our temperatures being marginally (23-175 K) hotter. The only noteworthy exception is J223811-104126, where we find an effective temperature of 5110 K, $\sim$536 K cooler than the 5646 K found by Wylie-de Boer et al. (2012). Similarly, Williams et al. (2011) report a hotter effective temperature of 5502 K from low-resolution spectra. This is the largest discrepancy we see in any of our standard or program stars.

Photometric temperatures only lend marginal weight towards our spectroscopic temperatures. If the Schlegel et al. (1998) dust maps are employed, then the Alonso et al. (1999) and Casagrande et al. (2010) relations estimate the effective temperatures to be between 5104 K

TABLE 5
Program Star Abundances

J221821-183424

Species	N	$\log \epsilon(X)$	σ_ϵ	[X/H]	[X/Fe]	σ
O I	2	7.50	0.04	−1.18	0.41	0.02
Na I	2	4.56	0.14	−1.68	−0.08	0.10
Mg I	4	6.55	0.37	−1.04	0.55	0.18
Al I	1	5.04	0.00	−1.41	0.18	...
Si I	5	6.28	0.08	−1.23	0.37	0.04
Ca I	4	4.97	0.04	−1.37	0.23	0.02
Sc I	0	...	...	...	...	...
Sc II	6	1.52	0.08	−1.63	−0.04	0.03
Ti I	0	...	...	...	...	...
Ti II	4	3.81	0.13	−1.14	0.45	0.07
V I	3	2.23	0.01	−1.70	−0.11	0.01
Cr I	11	3.74	0.07	−1.90	−0.30	0.02
Mn I	3	3.29	0.04	−2.14	−0.54	0.02
Fe I	52	5.91	0.09	−1.59	0.00	0.01
Fe II	13	5.90	0.05	−1.60	0.00	0.01
Co I	1	3.35	0.00	−1.64	−0.05	...
Ni I	5	4.61	0.15	−1.61	−0.01	0.07
Cu I	1	2.13	0.00	−2.06	−0.47	...
Zn I	2	3.15	0.11	−1.41	0.19	0.08

C2225316-14437

Species	N	$\log \epsilon(X)$	σ_ϵ	[X/H]	[X/Fe]	σ
O I	2	7.90	0.01	−0.79	0.48	0.01
Na I	3	5.09	0.17	−1.15	0.12	0.10
Mg I	4	6.98	0.24	−0.62	0.65	0.12
Al I	4	5.87	0.09	−0.58	0.68	0.04
Si I	5	6.96	0.15	−0.55	0.72	0.07
Ca I	4	5.50	0.04	−0.84	0.43	0.02
Sc I	0	...	...	...	...	...
Sc II	5	2.05	0.13	−1.10	0.17	0.06
Ti I	4	4.04	0.03	−0.91	0.36	0.01
Ti II	2	4.26	0.08	−0.69	0.58	0.06
V I	6	2.92	0.17	−1.01	0.26	0.07
Cr I	8	4.27	0.16	−1.37	−0.10	0.06
Mn I	3	4.14	0.05	−1.29	−0.02	0.03
Fe I	61	6.23	0.11	−1.27	0.00	0.01
Fe II	10	6.17	0.06	−1.33	−0.07	0.02
Co I	3	3.92	0.12	−1.07	0.20	0.07
Ni I	7	5.04	0.09	−1.18	0.09	0.03
Cu I	1	3.35	0.00	−0.84	0.43	...
Zn I	2	3.46	0.23	−1.10	0.17	0.17

J223504-152834

Species	N	$\log \epsilon(X)$	σ_ϵ	[X/H]	[X/Fe]	σ
O I	2	8.48	0.09	−0.21	0.46	0.07
Na I	3	5.76	0.12	−0.48	0.19	0.07
Mg I	3	7.50	0.24	−0.10	0.58	0.14
Al I	3	6.10	0.08	−0.35	0.32	0.05
Si I	5	7.11	0.10	−0.40	0.28	0.04
Ca I	4	6.03	0.04	−0.31	0.36	0.02
Sc I	0	...	...	...	...	...
Sc II	6	2.70	0.14	−0.45	0.23	0.06
Ti I	4	4.63	0.02	−0.32	0.36	0.01
Ti II	2	4.92	0.26	−0.04	0.64	0.19
V I	6	3.67	0.22	−0.26	0.41	0.09
Cr I	7	4.94	0.09	−0.70	−0.02	0.03
Mn I	3	5.08	0.10	−0.35	0.33	0.06
Fe I	64	6.83	0.12	−0.67	0.00	0.02
Fe II	12	6.82	0.07	−0.68	0.00	0.02
Co I	3	4.53	0.14	−0.46	0.21	0.08
Ni I	7	5.62	0.09	−0.60	0.08	0.03
Cu I	1	3.85	0.00	−0.34	0.33	...
Zn I	2	4.17	0.03	−0.39	0.28	0.02

J223811-104126

Species	N	$\log \epsilon(X)$	σ_ϵ	[X/H]	[X/Fe]	σ
O I	1	8.60	0.00	−0.09	0.14[a]	0.08
Na I	2	4.76	0.10	−1.48	−0.03	0.07
Mg I	3	6.49	0.42	−1.11	0.34	0.24
Al I	2	5.10	0.14	−1.35	0.10	0.10
Si I	3	6.38	0.04	−1.13	0.32	0.02
Ca I	4	5.30	0.03	−1.04	0.41	0.01
Sc I	0	...	...	...	...	...
Sc II	6	1.75	0.14	−1.40	0.05	0.06
Ti I	0	...	...	...	...	...
Ti II	4	3.83	0.09	−1.12	0.33	0.04
V I	1	2.42	0.00	−1.51	−0.06	...
Cr I	12	4.12	0.06	−1.52	−0.07	0.02
Mn I	3	3.55	0.04	−1.88	−0.43	0.02
Fe I	33	6.05	0.06	−1.45	0.00	0.01
Fe II	11	6.00	0.09	−1.50	−0.05	0.03
Co I	0	...	...	...	...	...
Ni I	2	4.82	0.04	−1.40	0.05	0.03
Cu I	1	2.39	0.00	−1.80	−0.35	...
Zn I	2	3.17	0.04	−1.39	0.06	0.03

C2306265-085103

Species	N	$\log \epsilon(X)$	σ_ϵ	[X/H]	[X/Fe]	σ
O I	2	8.09	0.15	−0.60	0.57	0.10
Na I	2	5.25	0.00	−0.99	0.18	0.00
Mg I	2	6.84	0.07	−0.76	0.41	0.05
Al I	4	5.56	0.08	−0.89	0.28	0.04
Si I	5	6.66	0.08	−0.85	0.32	0.03
Ca I	4	5.48	0.04	−0.86	0.31	0.02
Sc I	0	...	...	...	...	...
Sc II	6	2.18	0.15	−0.97	0.20	0.06
Ti I	4	4.06	0.03	−0.89	0.28	0.01
Ti II	3	4.21	0.36	−0.74	0.43	0.21
V I	4	2.88	0.06	−1.05	0.12	0.03
Cr I	4	4.20	0.26	−1.44	−0.27	0.13
Mn I	3	4.35	0.10	−1.08	0.09	0.06
Fe I	63	6.33	0.12	−1.17	0.00	0.01
Fe II	11	6.31	0.09	−1.19	−0.02	0.03
Co I	3	4.00	0.15	−0.99	0.18	0.08
Ni I	7	5.08	0.08	−1.14	0.03	0.03
Cu I	1	3.55	0.00	−0.64	0.53	0.00
Zn I	2	3.38	0.14	−1.18	−0.01	0.10

[a]Abundance derived from the permitted O I triplet instead of the forbidden [O I] lines, see §3.5.2

and 5367 K. Our spectroscopic temperature of 5110 K is closer to the Alonso et al. (1999) prediction, but not in disagreement with the Casagrande et al. (2010) relation. If we employ the reddening of $E(B-V) = 0.12$ that we have determined from interstellar Na D1 lines, the photometric temperatures increase slightly by ∼100 K, still within the uncertainties of the Alonso et al. (1999) scale, but in less agreement with the Casagrande et al. (2010) scale. We find the surface gravity for J223811-104126 to be 3.00±0.50, placing this star at the base of the red giant branch. Thus, our spectroscopic temperatures should be in slightly better agreement with the Alonso et al. (1999) scale for giant stars, rather than the Casagrande et al. (2010) dwarf/sub-giant scale. However, Williams et al. (2011) and Wylie-de Boer et al. (2012) find this star to be a sub-giant, with a surface gravity $\log g = 4.16$ and 4.60 respectively. In this scenario, their temperatures are 150 K and 300 K hotter than the Casagrande et al. (2010) prediction for Williams et al. (2011) and Wylie-de Boer et al. (2012) respectively. If our reddening is employed, then the Williams et al. (2011) and Casagrande et al. (2010) temperatures are in good agreement, yet still 175 K cooler than the Wylie-de Boer et al. (2012) measurement.

As a test, we set the temperature for J223811-104126 to be 5600 K – within the temperature regime reported by Williams et al. (2011) and Wylie-de Boer et al. (2012). The slopes in abundance with excitation potential and reduced equivalent width were large (how many dex), and in doing so we could not find a physical solution for this temperature. Thus, although photometric temperatures do not help in solving this discrepancy, and the reddening measured from the interstellar Na D1 line may have made it worse, our high-resolution spectra indicates that J223811-104126 has an effective temperature of 5110 K and is indeed a giant star.

In the Wylie-de Boer et al. (2012) study, the surface gravity was also determined during the χ^2 minimization process. Again, with the exception of J223811-104126, our surface gravities are largely in agreement. The only other noteworthy difference in surface gravity is for J221821-183424, where we find a lower gravity of $\log g = 0.80 \pm 0.30$ where Wylie-de Boer et al. (2012) find $\log g = 1.45 \pm 0.35\,\mathrm{cm\,s^{-2}}$. Given the difference in S/N and resolution between these studies, this difference is not concerning.

Wylie-de Boer et al. (2012) calculate microturbulence with the empirical relationships from Reddy et al. (2003) for dwarfs and Fulbright (2000) for giants. These relationships are based upon derived temperature and surface gravities. Our published microturbulence values agree excellently with the values presented in Wylie-de Boer et al. (2012), again with the exception of J223811-104126, where the difference in v_{mic} is directly attributed to the differences in other stellar parameters.

Of all the stellar parameters (T_{eff}, $\log g$, v_t and [Fe/H]), the metallicities between our two studies vary the most. Here we discuss the potential causes for these discrepancies. In the Wylie-de Boer et al. (2012) study, after the stellar parameters (T_{eff}, $\log g$, v_t, and an initial [Fe/H] estimate) had been determined, the authors synthesized Fe I and II lines to derive a final [Fe/H] abundance and an associated uncertainty. The spectrum synthesis code MOOG was used to derive abundances for individual Fe I and Fe II lines, and the Castelli & Kurucz (2003) stellar atmosphere models (the same ones used in this study) were employed. The median abundance of Fe I lines was taken as the overall stellar metallicity, scaled using the Grevesse & Sauval (1998) solar abundances.

The study of Wylie-de Boer et al. (2012) is of slightly lower resolution ($R = 25,000$ compared to $R = 28,000$ presented here), but with a much lower S/N ratio: ~ 25 compared to > 100 per pixel element achieved here. Given the lower spectral resolution and modest S/N in their study, there are fewer unblended absorption lines available. In fact, there are very few transitions present in their published line list: only 14 Fe I lines and 3 Fe II lines were available. For contrast, our metallicity determinations are based off X Fe I and Y Fe II lines. Given the metallicity of these stars and the spectral coverage (4120 to 6920 Å), it is somewhat surprising that there were not more unblended transitions available to Wylie-de Boer et al. (2012).

The line list employed in the Wylie-de Boer et al. (2012) study contained fewer lines, and employed different oscillator strengths than what we have used. The oscillator strengths in the Wylie-de Boer et al. (2012) study are astrophysical, and were derived from a reverse analysis using the Hinkle et al. (2003) solar atlas. Suspecting the metallicity discrepancy may be caused by the differing line lists, we have redone our analysis using the Wylie-de Boer et al. (2012) line list and their published stellar parameters. Indeed, we arrive at very similar metallicities to Wylie-de Boer et al. (2012). Without using their published stellar parameters a priori, with a 'blind' analysis using their line list we arrive at similar stellar parameters. However, we note that one Fe I transition at 6420.060 Å in their line list was not detected in any of our stars at the $3-\sigma$ level, even though the S/N at this point exceeds 120 per pixel element in every observation. Thus, for this comparative analysis a maximum of 13 Fe I and 3 Fe II lines were available to us.

Given the line list employed in the Wylie-de Boer et al. (2012) study, the overall data quality and the lack of suitable iron lines available for analysis, it appears the Aquarius stream stars have conspired to present a tight metallicity distribution function of $\sigma(\mathrm{Fe/H}) = 0.10$ dex – suggestive of a globular cluster origin. Our analysis of high-resolution spectra with high S/N reveals a much broader metallicity distribution for the stream. With just five stars – if we assume all our stars are members – we find the stream metallicity varies from $[\mathrm{Fe/H}] = -0.65$ to –1.60 dex. Although this is a small sample, we find the calculated median abundance and standard deviation to be $[\mathrm{Fe/H}] = X.XX \pm X.XX$ dex, more in line with the Williams et al. (2011) chemistry.

4.2. *The Aquarius Stream M.D.F.*

4.3. *The Na-O Relationship*

Extensive studies looking at stars in globular clusters have revealed variations in light-element abundances, most notably an anti-correlation in sodium and oxygen content Norris & Da Costa (1995); Carretta et al. (2009, and references therein). This pattern has been repeatedly demonstrated in all well-studied globular clusters, although the strength of the anti-correlation varies between systems. Between generations of stars within a globular cluster, oxygen is converted into nitrogen, reducing the overall oxygen abundance. Even though oxygen undergoes internal mixing during its evolution along the giant branch, it is now well established that any observed abundance variations due to such mixing is limited to Li, C, and N. Therefore, the observed anti-correlations in light elements required a different astrophysical explanation.

Carretta et al. (2009) defined three components of stars following this abundance pattern within a population: primordial, intermediate, and extreme components. The [Na/Fe] and [O/Fe] abundances for a given star defines which component it belongs to. Primordial (first-generation) stars are those with sodium and oxygen abundances which are similar to field stars of the same metallicity. For a well-studied system, stars with the lowest cluster [Na/Fe] abundances are characterised as primordial. An intermediate population – the second-generation of stars – will have super-solar sodium abundances, and demonstrate a slight depletion in oxygen content. The oxygen exhaustion rate is ultimately dependent on the star-formation history of the cluster environment. The intermediate population is sub-divided based on how much the O and Na abundances depart from the primordial population: stars with [O/Na]> -0.9 dex are classified as belonging to an extreme component of this Na-O pattern because they differ greatly from the primordial cluster abundance. The extreme O-depletion component has only been observed in a few clusters (preferentially more massive clusters with extended horizontal branches), indicating an long-lasting star-formation history in more massive clusters.

The exact astrophysical mechanism for oxygen depletion between generations of stars in globular clusters is still under debate. However, it is clear that this trend has been well-demonstrated empirically. Several hypotheses have been proposed in order to account for oxygen depletion between stellar generations, including massive binaries (de Mink et al. 2009) or fast-rotating massive stars (Decressin et al. 2007). While the exact procedure is yet to be fully characterized, we can describe the abundance variation as a simple oxygen depletion (or dilution) model with time. Through comparisons with existing globular clusters, we can still draw inferences on the star-formation history of a system from measuring sodium and oxygen in a sample of its stars.

It is clear that careful consideration must be given inferring star-formation histories from observed stellar abundances. In addition to the normal care afforded for measuring elemental abundances from high-resolution spectroscopic data, attention must be given to telluric absorption, contamination from nickel blends, and NLTE corrections when deriving oxygen abundances. Furthermore, when characterising the oxygen depletion rate – and hence the strength of the Na-O anti-correlation in a given cluster – it is vital to obtain observations for stars belonging to all three components (where possible). If only a primordial sample of stars in a globular cluster is observed, then their [Na/Fe] and [O/Fe] abundances will be indistinguishable from halo stars of a similar metallicity. In such a scenario, any inferred anti-correlation could equally be explained by intrinsic chemical scatter or observational uncertainties.

Wylie-de Boer et al. (2012) measured [Na/Fe] and [O/Fe] abundances for four of their six Aquarius stream members. This research has four stars in common with the Wylie-de Boer et al. (2012) study, but sodium and oxygen measurements exist for only three stars intersecting both samples. We have measurements for all of our stars, including J223811-104126, for which we ascertained an upper limit from the [O I] lines of [O/Fe] < 0.5 dex, and a corrected abundance of [O/Fe] $= 0.14$ from the O I triplet lines.

The Wylie-de Boer et al. (2012) measurements indicate two stars with solar levels of Na – identical to field star Na abundances for their metallicity – and two stars with super-solar sodium content. The sodium-enhanced stars exhibit no depletion of oxygen; the abundances do not demonstrate a classical Na-O anti-correlation. In fact, they have a slight positive relationship: their Na-enhanced stars show an increased oxygen content, contrary to an expected oxygen depletion between stellar generations within a globular cluster. This trend is drawn from a sample of only four stars – the same as this study if our upper limit for J223811-104126 is excluded.

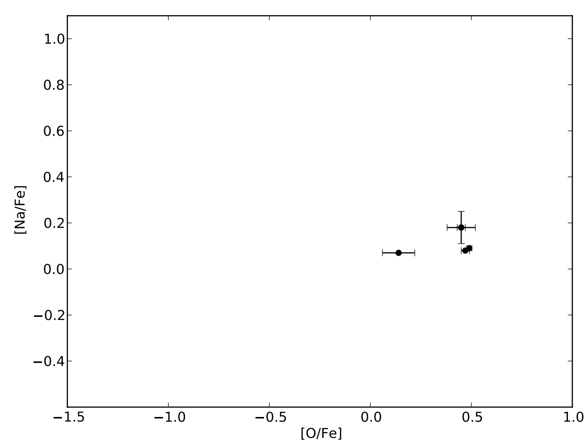

FIG. 5.— A plot showing [O/Fe] and [Na/Fe] for all Aquarius stream stars.

4.4. *The Al-Mg Relationship*

The effects of the Mg-Al cycle have been observed in globular cluster stars. The conditions required for these reactions are significantly higher than the CNO and Ne-Na cycle: temperatures of 70 MK are required for the Mg-Al channel instead of just 25 MK for the CNO/Ne-Na cycles **?**.

4.5. *The Na-Ni Relationship*

Detailed chemical studies of nearby disk stars have noted a correlation with [Na/Fe] and [Ni/Fe]. This relationship was first hinted in Nissen & Schuster (1997), where they found eight stars that were underabundant in [α/Fe], [Na/Fe] and [Ni/Fe]. Interestingly, the authors noted that stars at larger galactocentric radii were most deficient in these elements. Fulbright (2000) saw a similar signature: stars with low [Na/Fe] were only found at large ($R_\odot > 20\,\mathrm{kpc}$) distances. Nissen & Schuster (1997)

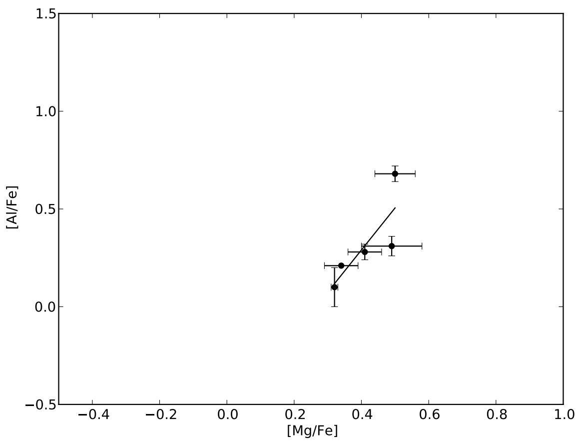

FIG. 6.— A plot showing [Mg/Al] for all Aquarius stream stars.

proposed that as the outer halo is thought to have been built up through the accretion of dSph satellites, then the Na-Ni pattern may be a chemical indicator of merger history in the galaxy.

With additional data from Nissen & Schuster (2011), the Na-Ni relationship was found to be slightly steeper than originally proposed. The pattern exists only for metal-rich stars $-1.5 < \mathrm{[Fe/H]} < -0.5$ dex, and is not seen in metal-poor dSph stars, providing a potentially useful indicator for investigating chemical evolution. However, it is crucial to note that although there are only a few dSph stars in the $-1.5 < \mathrm{[Fe/H]} < -0.5$ metallicity regime with [Na/Fe], [Ni/Fe] measurements, they agree reasonably well with the galactic trend.

The correlation between sodium and nickel content is the nucleosynthetic result of neutron capture in massive stars. As previously discussed, the total Na abundance is controlled by the neutron excess, which limits the production of ^{58}Ni during SN II events. When the inevitable supernova begins, the core photodissociates into neutrons and protons, allowing the temporary creation of ^{56}Ni before it decays to ^{56}Fe. A limited amount of ^{54}Fe is also formed, which is the main source of production for the stable ^{58}Ni isotope through α-capture. When the core dissociates, the quantity of ^{54}Fe (and hence ^{58}Ni) produced is dependent on the abundance of neutron-rich elements during the explosion. As ^{23}Na is a relatively plentiful neutron source with respect to other potential sources (like ^{13}C), the post-supernova ^{58}Ni abundance is driven by the pre-explosion ^{23}Na content. Recall that the total Na production primarily depends on the neutron excess. Thus, through populations of massive stars undergoing C-burning, a positive correlation between Na-Ni can be expected.

Stars originating in dwarf spheroidal galaxies and globular clusters have very different star formation histories. Consequently they exhibit chemical patterns that reflect their nucleosynthetic antiquity. Dwarf spheroidal stars do not demonstrate enhanced sodium or nickel, as there has been a relatively negligible linage of massive stars undergoing supernova. In contrast, globular cluster stars do have elevated Na, Ni contributions. This sharp contrast between dwarf spheroidal and globular cluster star chemistry is illustrated in Figure 7. Given the extended

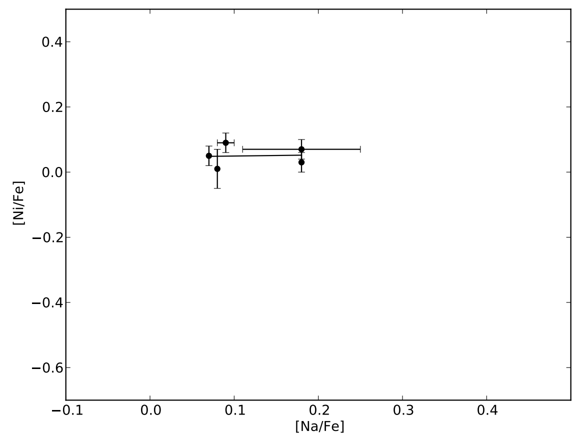

FIG. 7.— A plot showing [Na/Fe] and [Ni/Fe] for all Aquarius stream stars. TODO add dwarf/GC/disk stars on here.

star formation within the Milky Way disk, globular cluster stars and disk stars are indiscernible in the Na/Ni plane: they both show an extended contribution of massive stars. The most that can be inferred from the Na, Ni abundances of Aquarius stream stars is that their star formation history is less like a dwarf spheroidal environment, and more representative of an environment more like a globular cluster or the MW disk.

4.6. *Possible Progenitors*

Since the Aquarius stream is kinematically coherent, the default assumption is that the system has been accreted.

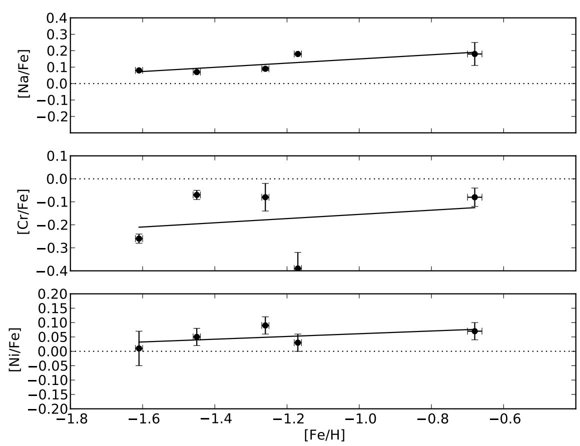

FIG. 8.— A plot showing [Na/Fe], [Cr/Fe], and [Ni/Fe] for all Aquarius stream stars.

REFERENCES

Allende Prieto, C., Lambert, D. L., & Asplund, M. 2001, ApJ, 556, L63

Alonso, A., Arribas, S., & Martínez-Roger, C. 1999, A&AS, 140, 261

TABLE 6
OBSERVED TARGETS

ID	α (J2000)	δ (J2000)	Air mass	S/N[a] (px^{-1})	V_{helio} (km s^{-1})
HD130694	14:50:17.1	–27:57:41.6	1.289	···	···
HD170642	18:32:21.0	–39:42:12.8	1.464	···	···
HD180928	19:18:59.6	–15:32:11.5	1.934	···	···
HD181342	19:21:03.9	–23:37:09.7	1.203	···	···
HD187111	19:48:39.3	–12:07:17.8	1.281	···	···
HD210049	22:08:22.8	–32:59:14.6	1.006	···	···
C2225316-145437	22:25:31.7	–14:54:39.6	1.033	···	···
J221821-183424	22:18:21.2	–18:34:28.3	1.026	···	···
J223504-152834	22:35:04.5	–15:28:34.9	1.047	···	···
J223811-104126	22:38:11.6	–10:41:29.4	1.218	···	···
C2306265-085103	23:06:26.6	–08:51:04.8	1.096	···	···
HD219615	23:17:10.7	+03:16:51.9	1.412	···	···

[a] S/N measured at 6000 Å for each target.

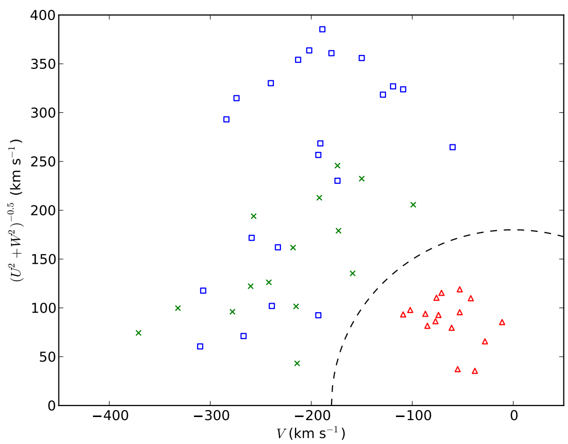

FIG. 9.— Toombre plot.

Asplund, M., Grevesse, N., Sauval, A. J., & Scott, P. 2009, ARA&A, 47, 481
Barber, C., Dobkin, D., & Huhdanpaa, H. 1996, ACM Transactions on Mathematical Software (TOMS), 22, 469
Bernstein, R., Shectman, S. A., Gunnels, S. M., Mochnacki, S., & Athey, A. E. 2003, in Society of Photo-Optical Instrumentation Engineers (SPIE) Conference Series, Vol. 4841, Society of Photo-Optical Instrumentation Engineers (SPIE) Conference Series, ed. M. Iye & A. F. M. Moorwood, 1694–1704
Burris, D. L., Pilachowski, C. A., Armandroff, T. E., Sneden, C., Cowan, J. J., & Roe, H. 2000, ApJ, 544, 302
Carretta, E., et al. 2009, A&A, 505, 117
Casagrande, L., Ramírez, I., Meléndez, J., Bessell, M., & Asplund, M. 2010, A&A, 512, A54
Castelli, F., & Kurucz, R. L. 2003, in IAU Symposium, Vol. 210, Modelling of Stellar Atmospheres, ed. N. Piskunov, W. W. Weiss, & D. F. Gray, 20P
de Mink, S. E., Pols, O. R., Langer, N., & Izzard, R. G. 2009, A&A, 507, L1
Decressin, T., Charbonnel, C., & Meynet, G. 2007, A&A, 475, 859
Frebel, A., Simon, J. D., Geha, M., & Willman, B. 2010, ApJ, 708, 560
Fulbright, J. P. 2000, AJ, 120, 1841
García Pérez, A. E., Asplund, M., Primas, F., Nissen, P. E., & Gustafsson, B. 2006, A&A, 451, 621
Gratton, R. G., Sneden, C., Carretta, E., & Bragaglia, A. 2000, A&A, 354, 169
Grevesse, N., & Sauval, A. J. 1998, Space Sci. Rev., 85, 161
Helmi, A., & White, S. D. M. 1999, MNRAS, 307, 495
Hinkle, K., Wallace, L., Livingston, W., Ayres, T., Harmer, D., & Valenti, J. 2003, in The Future of Cool-Star Astrophysics: 12th Cambridge Workshop on Cool Stars, Stellar Systems, and the Sun, ed. A. Brown, G. M. Harper, & T. R. Ayres, Vol. 12, 851–856
Munari, U., Sordo, R., Castelli, F., & Zwitter, T. 2005, A&A, 442, 1127
Munari, U., & Zwitter, T. 1997, A&A, 318, 269
Nissen, P. E., & Schuster, W. J. 1997, A&A, 326, 751
—. 2011, A&A, 530, A15
Norris, J. E., & Da Costa, G. S. 1995, ApJ, 441, L81
Norris, J. E., Ryan, S. G., & Beers, T. C. 1996, ApJS, 107, 391
Reddy, B. E., Tomkin, J., Lambert, D. L., & Allende Prieto, C. 2003, MNRAS, 340, 304
Robin, A. C., Reylé, C., Derrière, S., & Picaud, S. 2003, A&A, 409, 523
Schlegel, D. J., Finkbeiner, D. P., & Davis, M. 1998, ApJ, 500, 525
Sharma, S., Bland-Hawthorn, J., Johnston, K. V., & Binney, J. 2011, ApJ, 730, 3
Siebert, A., et al. 2011, AJ, 141, 187
Sneden, C. A. 1973, PhD thesis, The University of Texas at Austin.
Sobeck, J. S., et al. 2011, AJ, 141, 175
Steinmetz, M., et al. 2006, AJ, 132, 1645
Williams, M. E. K., et al. 2011, ApJ, 728, 102
Woosley, S. E., & Weaver, T. A. 1995, ApJS, 101, 181
Wylie-de Boer, E., Freeman, K., Williams, M., Steinmetz, M., Munari, U., & Keller, S. 2012, ApJ, 755, 35
Yong, D., Carney, B. W., & Teixera de Almeida, M. L. 2005, AJ, 130, 597
Zwitter, T., et al. 2008, AJ, 136, 421